Supporting Information

Womelsdorf et al. 10.1073/pnas.1114223109

SI Methods

The data used in this manuscript are largely the same as those used in Vinck et al. (1). Experiments were performed as described in detail in Vinck et al. (1) on three adult rhesus monkeys (Macaca mulatta). Before the experiment, each monkey was surgically implanted with a head post, a scleral search coil, and a recording chamber. Recordings were made from the opercular region of V1 (receptive field centers: 2–5° of eccentricity) and from the superior bank of the calcarine sulcus (receptive field centers: 8–12° of eccentricity). Recordings proceeded with 2–5 Quartz-insulated tungsten/platinum electrodes inserted independently into the cortex through transdural guide tubes with five precision hydraulic microdrives mounted onto an X-Y stage (MO-95; Narishige Scientific Instrument Laboratory). Spiking activity and the local field potential (LFP) were obtained by amplifying (1,000×) and band-pass filtering (multiunit activity: 700–6,000 Hz; LFP: 0.7–170 Hz) the recorded signals using a customized 32-channel headstage and preamplifier (headstage HST16o25; headstage and preamplifier from Plexon Inc. Additional 10× signal amplification was performed by onboard amplifiers (E-series acquisition boards; National Instruments). LFPs were acquired with a resolution of 1.0 ms. Spikes were detected online by amplitude thresholding. Spike events and corresponding waveforms were sampled at 32 kHz, and spike waveforms were recorded for 1.2 ms.

Visual Stimulation and Behavioral Task. Stimuli were presented as movies at 100 or 120 frames per second using a standard graphical board (GeForce 6600 series; NVIDIA). The cathode ray tube monitor used for presentation (CM813ET; Hitachi) was gamma corrected to produce a linear relationship between output luminance and gray values, and subtended a visual angle of 36 × 28° (1,024 × 768 pixels). At the beginning of each recording session, receptive fields were mapped using an automatic procedure, in which a bar was moved across the screen in 16 different directions (160 trials). Receptive field position was estimated from the global maximum of a response matrix, at a resolution of ∼6 min of arc. Subsequently, monkeys passively viewed drifting gratings during fixation of a small central fixation spot. Gratings had spatial frequencies ranging from 0.5 to 2.0 cycles per degree and velocities ranging from 0.5 to 3.0 degrees per second. Grating drift directions were generated randomly from a total of 16 directions (steps of 22.5°). The stimuli were centered over the receptive fields within a circular aperture of 8.0°. After the monkey acquired fixation, there was a prestimulus baseline of 800–1,000 ms, after which the stimulus was presented for 800–1,400 ms. To obtain a reward, monkeys had to release the lever within 500 ms after the color change. Trials were aborted upon fixation breaks, or when the lever was released before the color change. Eye position was monitored continuously by a search coil system (DNI; Crist Instruments) with a temporal resolution of 2 ms.

Spike-LFP Phase Locking and Spike Phase Analysis. Centered around each spike recorded on one electrode, the respective data segments of the LFPs recorded on the other electrodes were cut out. For the sustained response period starting 0.25 s after stimulus onset we used segments of 0.15 s. The mean of each LFP data segment was subtracted, to avoid leakage of the dc component into neighboring frequencies. Each LFP data segment was multiplied by a Hanning window before Fourier transforming it, giving the spike-triggered LFP spectrum. For a given frequency and a given spike, we determined the circular mean of the spike phases across all of the LFPs from the different electrodes. We measured phase consistency by means of the PPC, which is an unbiased estimator of the squared spike-LFP phase-locking value (2). For example, a PPC value of 0.01 corresponds approximately to a phase-locking value of 0.1. The statistical significance of spike-LFP phase locking was assessed by means of the Rayleigh test ($\alpha = 0.05$).

To compute spike-LFP phase locking for the lower frequencies, we computed spike phases relative to the 0.2–1.0 s LFP segment from the same trial, or relative to the average LFP 0.2–1.0 s segment from all trials with an identical stimulus, excluding the same trial. This computation gave a frequency resolution of 1.25 Hz. Finally, we computed spike phases relative to the time point 0 s, with the phase value defined as $2\pi tf$ (*SI Results*).

Quantification of Orientation Tuning. We quantified orientation selectivity (OSI) by considering the neuronal response variation across all orientations by calculating [1 − circular variance]. This measure reflects the resultant vector length of the spike rates across orientations and has been validated in previous studies (3–5). The definition of the OSI is as follows: let r_m $(m = 1, 2, \ldots, 8)$ be the empirically observed average firing rate (no. of spikes per second) over trials when the mth stimulus orientation θ_m = (0°, 22.5°,..., 157.5°) was presented. Stimulus orientation is a circular variable with a period of 180°. Define the normalized firing rates as $w_m \equiv r_m / \sum_{m=1}^{8} r_m$, such that $0 \le w_m \le 1$ and $\sum_{m=1}^{8} w_m = 1$. To apply circular statistics to the orientation vs. firing rate data, we need to transform the orientation variable to a circular variable that spans the [–π, +π] interval, (i.e., for every m, we define $\tilde{\theta}_m = \theta_m 2\pi/180$ radians) (Fig. S4 *A* and *B*). The estimated OSI is then defined as

$$\hat{S} \equiv \left| \sum_{m=1}^{8} w_m e^{i\tilde{\theta}_m} \right|, \qquad \text{[S1]}$$

[i.e., the magnitude of the vector sum obtained by vector addition (in the complex plane) of the eight normalized vectors $w_m e^{i\tilde{\theta}_m}$]. The OSI takes values within the interval [0, 1], with a value of 0 indicating absence of orientation selectivity and a value of 1 maximum orientation selectivity. The computation of the OSI is illustrated in Fig. S4.

Effect of Spike Rate and Spike Count on OSI. For a large number of trials (or more generally, for long observation times), the OSI is invariant to a linear scaling of the firing rate. As the number of trials grows, the OSI converges to what we call the true OSI (i.e., the population statistic whose estimate we seek),

$$S \equiv \left| \sum_{m=1}^{8} \mathrm{E}\{w_m\} e^{i\tilde{\theta}_m} \right|, \qquad \text{[S2]}$$

where E{} is the expected value operator. Asymptotically, as the number of trials (and the spike count) grows, the equality $\mathrm{E}\{w_m\} = \mathrm{E}\{r_m\} / \sum_{m=1}^{8} \mathrm{E}\{r_m\}$ holds. If we scale the firing rates for all of the eight orientations by a constant factor c, then this scaling factor falls away by division, because the equality

$$\mathrm{E}\{w_m\} = \frac{c\mathrm{E}\{r_m\}}{\sum_{m=1}^{8} c\mathrm{E}\{r_m\}} = \frac{\mathrm{E}\{r_m\}}{\sum_{m=1}^{8} \mathrm{E}\{r_m\}} \qquad \text{[S3]}$$

holds, showing that in the asymptotic sampling regime, the OSI is invariant to a linear scaling of the firing rate.

However, for a small number of trials (or more generally a short observation time and, correspondingly, small spike counts) the empirically observed normalized firing rate weights will deviate from $E\{w_m\}$ with some statistical error. From Jensen's inequality, which states that $h(E\{x\}) \leq E\{h(x)\}$ if $h(x)$ is a convex function, it follows that the OSI estimate is a positively biased quantity, i.e.

$$S = \left| E\left\{ \sum_{m=1}^{8} w_m e^{i\tilde{\theta}_m} \right\} \right| \leq E\{\hat{S}\} \qquad \text{[S4]}$$

because the function $h(x) = |x|$ is convex.

Using simulations, we directly addressed the question how the OSI is affected by subsampling spike trains (as we do by binning the spikes into gamma-phase bins). We generated firing rates for every orientation by using the circular von Mises density, a common model of orientation tuning (6). The von Mises density for a particular stimulus orientation was defined as

$$f(\tilde{\theta}_m|\mu,\kappa) \equiv \frac{e^{\kappa\cos(\tilde{\theta}_m - \mu)}}{2\pi I_0(\kappa)}, \qquad \text{[S5]}$$

where $I_0(\kappa)$ is the modified Bessel function of order 0, a mere normalization factor ensuring that the integral of the von Mises density (across the $[-\pi, +\pi]$ interval) amounts to 1, μ is the mean phase, and κ is the concentration parameter that for this particular application controls the OSI, with low and high OSI values for small and large values of κ, respectively. We first constructed a large pool of spikes such that the OSI for this large pool of spikes converged with very small error to its true value (i.e., the value based on the expected spike count). For a given level of the concentration parameter κ, we multiplied the circular von Mises density, for every stimulus orientation, by a factor of 30, such that $E\{r_m\} = 30 \cdot f(\tilde{\theta}_m)$ and generated a large pool of spikes ($n = 38{,}620$) according to this model by multiplying $E\{r_m\}$ by 1,000 and rounding the resulting number. The factors 30 and 1,000 are arbitrary and merely ensure that the initial pool of spikes is large. We then drew a random subset of spikes of size M from this sample of 38,620 spikes, and computed the OSI for this subset. We repeated this subsampling 1,000× to obtain an estimate of the expected OSI, [i.e., $E\{\hat{S}\}$], and the variance of the OSI estimate, [i.e., $\mathrm{Var}\{\hat{S}\}$], given the subsample size M and the tuning level κ. The distribution of OSIs is shown for various levels of the tuning parameter κ (0.01, 1, and 5) and subsample sizes M = 40, 200, 10^3 and 10^4 (Fig. S5 *A*–*C*). The variance of the OSI estimates was particularly high when the "true" OSI was small, and was higher when we drew a smaller subset M. Fig. S5*D* shows that the expected OSI value was higher when M was small. The explanation for this finding is that if we draw a smaller subsample, the variance of the OSI estimates increases. If the true OSI (i.e., computed over the large pool of spikes) is near zero, then increasing the variance will push the expected OSI value away from zero, because the OSI is bound from below by zero. If the true OSI is near 1, however, then the variance of the OSI estimates is very low, such that subsampling will hardly push the expected OSI value away from 1. It is interesting to note that this positive bias in OSI estimation behaves similarly to the bias of the phase-locking value and coherence estimates (2), and our strategy of controlling for this bias by using bins of variable width is similar to our fixed sample size phase-locking value estimate (1, 2).

Interpretation of Phase-Dependent OSI in Terms of Spike Densities. At every phase $\gamma \in [-\pi, \pi]$ in the gamma cycle, there is a spike density (i.e., an expected number of spikes per second). The average spike density across stimuli, [i.e., the density that is not conditional on any particular stimulus, is denoted as $g(\gamma)$]. The expected number of spikes in a small phase bin of size Δ (in seconds) equals approximately $\Delta g(\gamma)$. We can also define the spike density conditional on the observation of a particular stimulus orientation θ_m, denoted as $g(\gamma|\theta_m)$. The spike densities can be normalized across stimuli such that they sum to 1, [i.e., $\tilde{g}(\gamma|\theta_m) \equiv g(\gamma|\theta_m)/\sum_{m=1}^{8} g(\gamma|\theta_m)$ for every m]. By applying Eq. 2, we can define the gamma phase-dependent OSI as

$$S(\gamma) \equiv \left| \sum_{m=1}^{8} \tilde{g}(\gamma|\theta_m) e^{i\tilde{\theta}_m} \right|. \qquad \text{[S6]}$$

Because the number of trials is limited, we need to estimate $g(\gamma|\theta_m)$ by averaging over a range of phases. This was performed using eight nonoverlapping phase bins. The advantage of this discrete binning approach over a circular kernel-smoothing approach is that the overall number of spikes across orientations can be controlled by varying the bin widths.

Frequency Specificity of Phase-Dependent Rate Tuning. To test for the frequency specificity of phase-dependent orientation tuning, we calculated OSI for each phase-binning type across frequencies from 20 to 120 Hz. For each phase-binning type we then derived for each frequency a modulation depth indexing the orientation tuning across phase bins. For binning the gamma cycle into phase bins with equal bin width or equal spike number per phase bin (Fig. 2 *A* and *B*), we derived the modulation depth of a cosine (peak-to-trough) fit to the OSI as a function of the phase-bin centers. Larger cosine modulation depth indicates that the OSI is modulated across phase bins. Statistical significance of tuning was assessed by a permutation test. We calculated a random distribution of $n = 500$ tuning indices by randomly shuffling the phase bin assignment before obtaining the cosine modulation depth. This random distribution shows tuning under the null hypothesis that the OSI would not vary across phase bins. The observed tuning index was considered significant when the probability to observe it in the null distribution was $P < 0.01$.

Noise Correlations as a Function of Gamma Power and Phase. We calculated noise correlations as the linear (Pearson) correlation coefficient between the firing rates of the units at different electrodes. All noise correlations were computed for trials with identical stimuli (direction of moving grating). To avoid any influence from the drift of the grating stimulus on our correlations, correlations were computed for firing rates that were defined for the complete trial period (from >200 ms after stimulus onset). For the first analysis, we calculated noise correlations for subsets of trials median split according the LFP gamma-band power. For the second analysis, we binned for a given neuron spike phases into nonoverlapping bins containing equal numbers of trials. We then computed noise correlations across trials between the spike rates within a particular phase bin and the spike rates of a simultaneously recorded neuron that were defined across all phase bins.

SI Results

All analyses in the main text concentrated on rhythmic neuronal synchronization >20 Hz. Orientation selectivity may also be dependent on the phase of spiking relative to slower oscillations; we investigated this in separate analyses. All low-frequency analyses were restricted to the first two monkeys, because the trials for the third monkey were too short (0.8 s, 0.6 s after excluding the onset transient) to obtain sufficient spectral resolution. For the epoch from 0.2 s to 1 s after stimulus onset, spikes were locked to LFP oscillations in the 1- to 3-Hz range (Fig. S2 *A* and *B*, black lines), with significant phase locking observed for 13 of 47 units at 2.5 Hz (monkey JE) and 1.25 Hz (monkey LI; Rayleigh test at $P = 0.05$). Interestingly, spikes were more strongly locked to the 1- to 3-Hz component of the stimulus-locked LFP-average, which was computed over all trials with

identical stimulus direction (Fig. 2 *A* and *B*, blue lines). Significant delta phase locking was observed for 19 of 47 units at 2.5 Hz (monkey JE) and 1.25 Hz (monkey LI; Rayleigh test at $P = 0.05$). Finally, spike phases were even more strongly locked to stimulus onset (Fig. 2 *A* and *B*, red lines). Now, 38 of 47 units reached significant locking values at 2.5 Hz (monkey JE) and 1.25 Hz (monkey LI; Rayleigh test at $P < 0.05$). Thus, the observed delta oscillation was predominantly a stimulus-evoked rhythm. Further analyses were restricted to the individual monkeys' delta frequencies, with the spikes' delta phases defined relative to stimulus onset. Orientation tuning was significantly modulated with delta phase for the lower frequencies (Fig. 2 *C* and *D*). We observed a strong cosine modulation of OSI with delta phase (mean explained variance $R^2 = 0.47$, $P < 0.001$), significant for 29.8% cells (14/47; at $P = 0.05$, permutation test). Surprisingly, the phases at which the OSI peaked were not clustering across units (Rayleigh test, $P = 0.83$). Thus, the modulation of OSI with delta phase was dissociated from the modulation of firing rate with delta phase. Finally, no linear relationship between noise correlation and the delta oscillation power was observed; noise correlation did not significantly differ between high and low delta power trials (mean difference = −0.03, Wilcoxon signed rank test, $P = 0.33$, 42 pairs). Finally, although highest noise correlation was found for the mean delta-phase bin (0.04 ± 0.021 SEM), none of the respective tests with the other phase bins were significant (permutation test). Across cells, OSI was not significantly related to the strength of delta locking. We performed a multiple linear regression analysis with Z-score–transformed delta PPC values and Z-score–transformed gamma PPC values as two predictors (including all neurons). Z-score–transformed gamma locking significantly predicted tuning ($P < 0.001$), but delta locking did not ($P = 0.46$). Also, delta locking and gamma locking were not significantly linearly related ($R = 0.21$, not significant).

1. Vinck M, et al. (2010) Gamma-phase shifting in awake monkey visual cortex. *J Neurosci* 30:1250–1257.
2. Vinck M, van Wingerden M, Womelsdorf T, Fries P, Pennartz CM (2010) The pairwise phase consistency: A bias-free measure of rhythmic neuronal synchronization. *Neuroimage* 51:112–122.
3. Dragoi V, Sharma J, Sur M (2000) Adaptation-induced plasticity of orientation tuning in adult visual cortex. *Neuron* 28:287–298.
4. Ringach DL, Shapley RM, Hawken MJ (2002) Orientation selectivity in macaque V1: Diversity and laminar dependence. *J Neurosci* 22:5639–5651.
5. Shapley R, Hawken M, Ringach DL (2003) Dynamics of orientation selectivity in the primary visual cortex and the importance of cortical inhibition. *Neuron* 38: 689–699.
6. Swindale NV (1998) Orientation tuning curves: Empirical description and estimation of parameters. *Biol Cybern* 78:45–56.

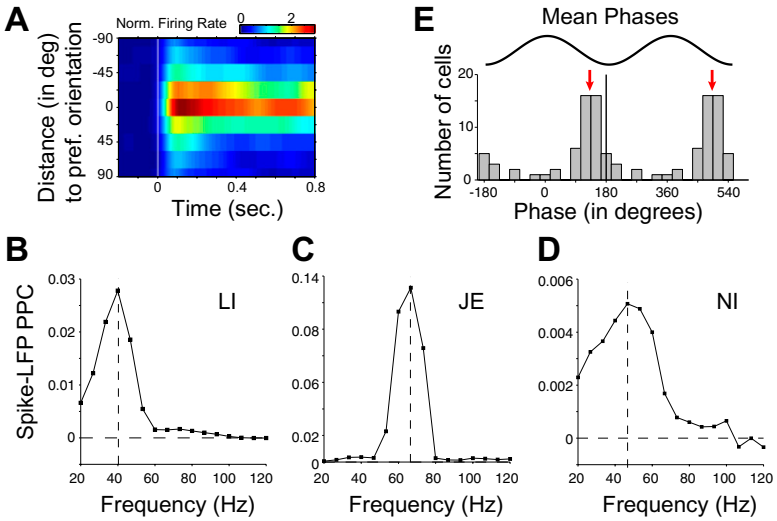

Fig. S1. Spike rate and spike-LFP phase-locking spectra. (*A*) Average normalized spike density across time for eight stimulus orientations sorted according to individual cells' preferred stimulus orientation before averaging. (*B–D*) Average spike-LFP PPC spectra plotted as function of frequency for three monkeys. Dashed lines denote frequency with peak phase locking in the gamma frequency band. The spectra of stimulus-induced LFP power change for the three monkeys have been published in Lima et al. (1). For monkeys LI and JE, there was a perfect match between gamma peaks in stimulus-induced gamma and spike-LFP PPC. For monkey NI, there was a higher diversity of peak gamma frequencies in the LFP power spectrum, as can be seen from the respective figures 7 and 9 in ref. 1. This diversity was most likely due to the fact that some recordings had been performed in the operculum and others in the calcarine sulcus [see Lima et al. (1) for details]. The ~50-Hz peak in the spike-LFP PPC spectrum shown here can be seen in a large number of LFP power change spectra of monkey NI (1, 2). (*E*) Histogram of mean phases across spike-LFP pairs at the gamma frequency with peak PPC values. Gamma frequencies were defined for each monkey separately as indicated in *B–D*. Subsequently, spike-LFP pairs were pooled across monkeys. The red line denotes the average phase at which spikes locked to the LFP across pairs.

1. Lima B, Singer W, Chen NH, Neuenschwander S (2010) Synchronization dynamics in response to plaid stimuli in monkey V1. *Cereb Cortex* 20:1556–1573.
2. Lima B, Singer W, Neuenschwander S (2011) Gamma responses correlate with temporal expectation in monkey primary visual cortex. *J Neurosci* 31:15919–15931.

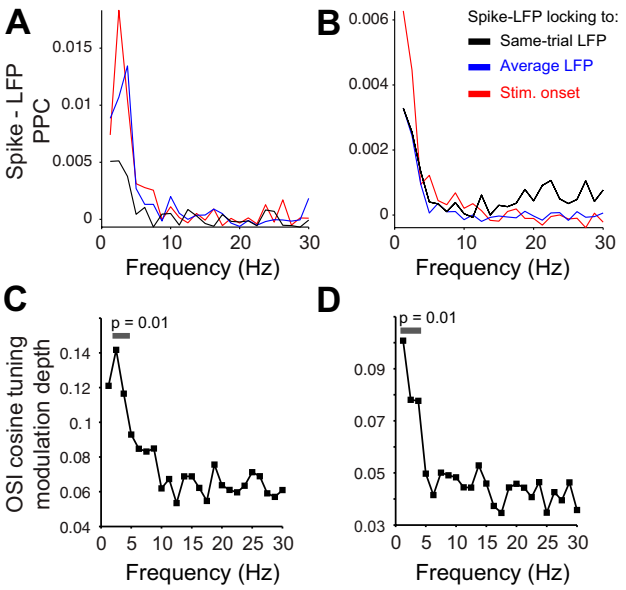

Fig. S2. Low-frequency rhythms and orientation selectivity. (*A* and *B*) PPC (*y* axis) as a function of frequency (*x* axis) for monkeys JE (*A*) and LI (*B*), shown separately for spike phases defined relative to the same-trial LFP (black), the average LFP from different trials with identical visual stimulation (blue), and stimulus onset (red). (*C* and *D*) Depth of phase bin-dependent modulation of OSI (*y* axis) as a function of frequencies (*x* axis). Phase bins contained equal spike counts per bin. OSI modulation depth indexes the peak-to-trough modulation depth of a cosine fit to the OSI as a function of phase bins per frequency. Gray bars on top of each panel highlight frequencies with statistically significant phase bin-dependent tuning (see *Methods* and *SI Results* for details).

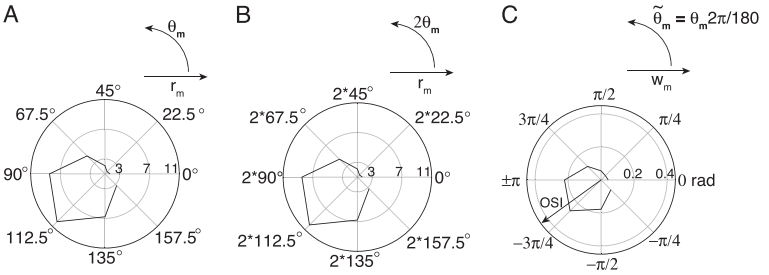

Fig. S3. Computation of OSI. (*A*) Polar representation of stimulus orientations θ_m $(m = 1, 2, \ldots, 8)$ with average firing rates r_m. Firing rates were defined, for this particular illustrative example, by first computing the circular von Mises density $f(\tilde{\theta}_m \mid \mu, \kappa)$ (Eq. 5, *SI Methods*). The firing rate was then (the parameters were arbitrarily chosen for this particular example) defined as $r_m = 30 \cdot f(\tilde{\theta}_m \mid \mu = 1.2\pi, \kappa = 1)$. (*B*) Polar representation of eight stimulus orientations mapped onto the [0, 360°] interval, and associated firing rates r_m. (*C*) Polar representation of eight orientations mapped onto the [–π, +π] interval ($\tilde{\theta}_m$), with associated normalized firing rates $w_m = r_m/(\sum_{m=1}^{8} r_m)$ that sum to 1. The arrow represents the vector sum; its magnitude corresponds to the OSI, which attains values in the [0, 1] interval. In this particular simulated example, it assumes a value of 0.45.

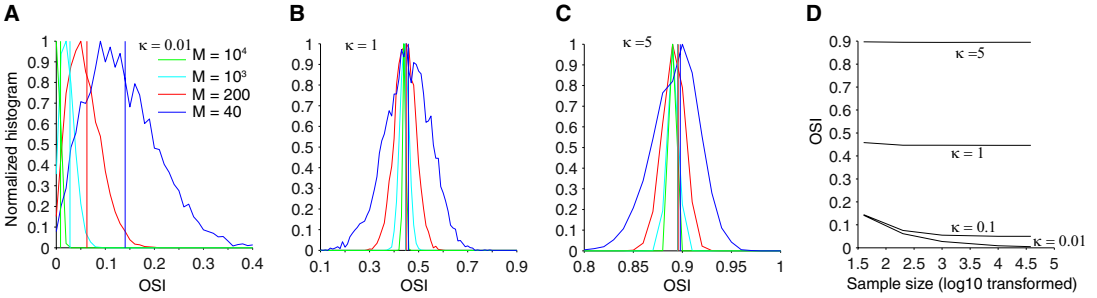

Fig. S4. Effect of subsampling spike trains on the OSI. (*A*) Normalized histogram of OSI values (normalized by dividing by maximum histogram count) obtained from taking a random subsample of spikes from all of the available spikes (n = 38,620). Different lines correspond to different sizes of the subsample. Vertical lines indicate the expected OSI value for a given subsample. Firing rates r_m were generated according to a von Mises model $30 \cdot f(\tilde{\theta}_m \mid \mu, \kappa)$ (Eq. 5, *SI Methods*), with the concentration parameter κ = 0.01, and the number of spikes equal to 1,000 × r_m (rounded). The chosen parameters 30 and 1,000 are arbitrary and merely control the initial size of the pool of spikes. (*B*) Same as in *A*, but now with the von Mises concentration parameter κ = 1. (*C*) Same as in *A* and *B*, but now with κ = 5. (*D*) Expected OSI value (*y* axis) as a function of subsample size (*x* axis) for different levels of the von Mises parameter κ (*Bottom* to *Top*: κ = 0.01, 0.1, 1, 5).

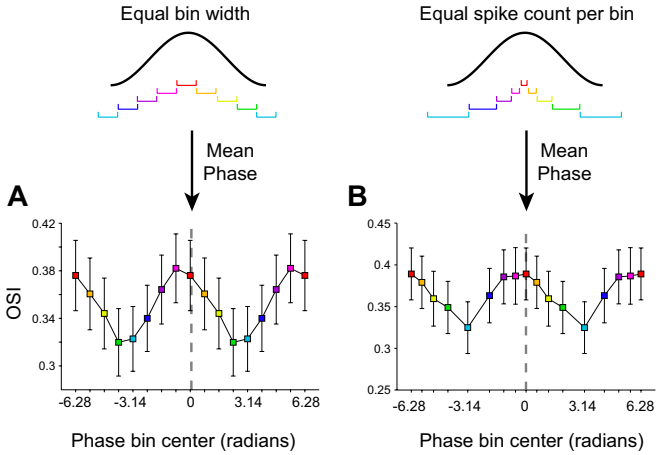

Fig. S5. Population results for gamma phase-dependent orientation selectivity. (*A* and *B*) Raw, group-average OSI [1 − circular variance] for phase-dependent spike counts for each phase-binning type. The *x* axes denote the phase-bin centers. Arrows indicate the mean phase bin. Error bars denote SEM.